

16 **Abstract**

17 It is estimated that 2 billion people will move to cities in the next 30 years, many of which
18 possess high seismic risk, underscoring the importance of reliable hazard assessments. Current
19 ground motion models for these assessments typically rely on an extensive catalogue of events to
20 derive empirical Ground Motion Prediction Equations (GMPEs), which are often unavailable in
21 developing countries. Considering the challenge, we choose an alternative method utilizing
22 physics-based (PB) ground motion simulations, and develop a simplified decomposition of
23 ground motion estimation by considering regional attenuation (Δ) and local site amplification
24 (A), thereby exploring how much of the observed variability can be explained solely by wave
25 propagation effects. We deterministically evaluate these parameters in a virtual city named
26 Tomorrowville, located in a 3D layered crustal velocity model containing sedimentary basins,
27 using randomly oriented extended sources. Using these physics-based empirical parameters (Δ
28 and A), we evaluate the intensities, particularly Peak Ground Accelerations (PGA), of
29 hypothetical future earthquakes. The results suggest that the estimation of PGA using the
30 deterministic $\Delta - A$ decomposition exhibits a robust spatial correlation with the PGA obtained
31 from simulations within Tomorrowville. This method exposes an order of magnitude spatial
32 variability in PGA within Tomorrowville, primarily associated with the near surface geology and
33 largely independent of the seismic source. In conclusion, advances in PB simulations and
34 improved crustal structure determination offer the potential to overcome the limitations of
35 earthquake data availability to some extent, enabling prompt evaluation of ground motion
36 intensities.

37

38 **Plain Language Summary**

39 Numerous cities in earthquake-prone regions of the Global South are currently experiencing
40 rapid growth, which poses a significant risk to their populations in the upcoming years. The
41 attainment of effective urban planning, which takes earthquake vulnerabilities into account,
42 typically needs access to long-term earthquake recordings for projecting ground shaking through
43 to future seismic events. Regrettably, the scarcity of earthquake monitoring disproportionately
44 hampers this potential in the Global South, resulting in the utilization of ground motion data
45 from distant locations across the globe. This approach, however, comes with notable limitations

46 and contributes to the large uncertainty surrounding predictions of ground shaking. We approach
47 this challenge by employing state-of-the-art physics-based simulation techniques that can use
48 hypothetical earthquakes and numerically solve the seismic wave propagation through the
49 Earth's crust. Our study shows that even when a comprehensive earthquake database is lacking,
50 it is feasible to generate reasonably accurate predictions of the spatial variability in expected
51 ground motions using high-resolution local geological information. We emphasize that in cases
52 where urban planning choices need to be formulated for a city characterized by diverse
53 geological features, substantial investments in the measurement of subsurface properties can
54 prove valuable.

55

56 **1 Introduction**

57 Seismic hazard analysis informs building codes constraining construction of new development in
58 earthquake prone areas. The hazard is a result of the interaction between a range of individually
59 heterogeneous fields and processes, leading to deep complexity in even the simplest relationships
60 (Baker et al., 2021; Bradley, 2019; Kramer, 1996; Kramer & Mitchell, 2006; Mcguire, 2008;
61 Stirling, 2014; Stirling et al., 2012). Measures of ground shaking intensity, for example, show an
62 expected systematic decrease with distance between the observation and source, but the
63 systematics are overprinted by the interactions between the complexities of the event and the
64 crustal volume explored by the seismic wave train. The result is high amplitude variability in the
65 observed intensity. Note that the uncertainty in the observations, in either intensity or distance,
66 makes only a small contribution to this variability; the variability is an intrinsic part of the
67 process.

68 Consider a series of events recorded at large number of sensors. In the commonly applied
69 approach, the analyst chooses a functional form for the systematic decay of intensity and uses
70 some fitting procedure to estimate its parameters. The resulting model is commonly known as a
71 Ground Motion Model (GMM) (Douglas & Aochi, 2008; Douglas & Edwards, 2016a, 2016b),
72 and takes the form:

$$73 \quad \ln IM = \mu_{\ln IM} + \sigma_{\ln IM} \cdot \epsilon \quad (1)$$

74 Where, IM is the required intensity measure, $\mu_{\ln IM}$, is the estimated mean-field intensity, $\sigma_{\ln IM}$,
75 is an estimate of the variability around the mean which is usually assumed to conform to a log-
76 normal distribution and ϵ is the standard normal variate.

77 It is important to note that the $\mu_{\ln IM}$ term does not just describe the attenuation of intensity with
78 distance. Common forms of $\mu_{\ln IM}$ attempt to parameterize descriptions of the physics of the
79 entire process including source properties, such as focal mechanism and their resulting
80 directivity, as well as the local response of the site using estimates of V_{s30} (time-averaged shear-
81 wave velocity in the top 30m) and κ (high frequency attenuation parameter) for example (Aki,
82 1993; Borchardt & Glassmoyer, 1992; Bradley, 2011; Hough & Anderson, 1988; Kaklamanos et
83 al., 2013; Shi & Asimaki, 2017). Expressions for $\mu_{\ln IM}$ in current GMMs include numerous
84 parameters, use advanced statistical techniques to fit these complex functions, and represent a
85 practical approach to a fundamentally intractable problem (Douglas & Edwards, 2016a).

86 In practice, an ergodic assumption is invoked in GMM development by aggregating the data
87 from multiple spatial locations that is assumed to be equivalent to the distribution in time
88 (Anderson & Brune, 1999). However, with the increasing data for a particular tectonic area, the
89 non-ergodic or partial non-ergodic approaches are favoured which modify $\mu_{\ln IM}$ and $\sigma_{\ln IM}$ based
90 on calibration with the local data that is available (Bradley, 2015; Rodriguez-Marek et al., 2014;
91 Stewart et al., 2017). It is observed that major component of ground motion amplification can be
92 associated with the site-specific effects (Bazzurro & Cornell, 2004a), hence, the general practice
93 in GMM development is dominated by using near-surface site-specific parameters (for example
94 V_{s30} and κ). It is suggested that these near-surface parameters might exhibit strong correlations
95 with geological features at greater depths, like basin depth parameters (Z_{xx}) (Chiou & Youngs,
96 2014; Kamaï et al., 2016; Tsai et al., 2021), and consequently the amplification. However,
97 opposing studies show that the amplification patterns might not necessarily correlate with these
98 parameters (Castellaro et al., 2008; Mucciarelli & Gallipoli, 2006; Pitilakis et al., 2019), for
99 example, sites with velocity profiles which are not monotonically increasing with depth. This
100 highlights the necessity to investigate more regional geological structure to better understand the
101 complexities of ground motion amplification.

102 Recently, the advances in computational capabilities and understanding the physical processes
103 have made it possible to use physics-based (PB) simulations for modelling ground motions
104 (Bradley, 2019; Graves & Pitarka, 2010; Smerzini & Villani, 2012; Taborda et al., 2014). PB
105 simulations are carried out by numerical modelling of the entire process of rupture
106 characterization and seismic wave propagation through the potentially complex Earth's crust.
107 However, the high computational cost and complex input requirements associated with them
108 restrict the large-scale usage of these methods, particularly in 3D. As a consequence the relative
109 contribution of these processes to the total observed variability has been relatively unexplored
110 compared to that of local shallow (decametre) site conditions.

111 The importance of robust ground motion modelling is particularly important during the current
112 unprecedented global urbanization. The United Nations Human Settlements Programme (UN-
113 Habitat) forecasts that by 2050 some 2 billion new citizens will move to urban centers so that, by
114 then, some 68% of the world's population will live in cities (UN-Habitat, 2022). It is estimated
115 that 95% of this urbanization will happen in the global south. Urban population growth is often
116 accommodated by rapid urban expansion in areas with well-documented seismic risk. The
117 problems of understanding and reducing disaster risk in such rapid development are significant,
118 and while this expansion presents a major global challenge, it also provides a time-limited
119 opportunity to provide evidence-based decision support for this new development (UNISDR,
120 2015). Efforts in earthquake risk reduction through urban planning guided by high-resolution
121 ground-motion modelling, could reduce disaster risk for hundreds of millions of these future
122 citizens. This approach also provides a cost-efficient method by concentrating on new
123 constructions, where the expenses related to implementing effective earthquake-resistant design
124 and construction are significantly lower compared to the costs of retrofitting at a later stage.

125 Two immediate problems emerge in enacting the scheme described above in this context. Firstly,
126 understanding ground motion requires extensive seismic databases recording appropriate
127 measures of intensity from a large number of earthquakes, recorded at a network of sensors in
128 the area of interest, for example, PEER-NGA databases (Ancheta et al., 2014; Atkinson &
129 Boore, 2006; Spudich et al., 2013). Such catalogues necessitate the deployment of seismometers
130 for many years even in the most seismically active areas that is not possible to address the
131 current time-critical problem (Freddi et al., 2021). Secondly, urban development projects require
132 hazard information at unusually high resolution. Urban flood modelling and landslide

133 susceptibility estimates, for example, typically strive to use digital terrain models with 2-meter
134 resolution supplemented by high-resolution geotechnical assessments (Jenkins et al., 2023).
135 Seismic intensity also varies significantly over the scale of interest for urban planning,
136 particularly where development is planned over sedimentary basins or near to coasts or rivers
137 with strong spatial contrasts in sub-surface seismic velocity (Bielak et al., 1999; see also, Cadet
138 et al., 2011; Foti et al., 2019).

139 Modellers have recognized the difficulties associated with the variability of ground motion at
140 small scales, which can be attributed to local geological factors e.g. sedimentary basins (Graves
141 et al., 1998; Pilz et al., 2011; Zhu et al., 2018), surface topography (Lee et al., 2009; Maufroy et
142 al., 2012; G. Wang et al., 2018), and soil conditions (Bazzurro & Cornell, 2004b; Cramer, 2003;
143 Torre et al., 2020). In this study, we focus on the effects only due to the sedimentary basins,
144 which are known to enhance the amplitude and duration of seismic waves through frequency-
145 dependent focusing, trapping and resonance (Frankel, 1993; Yomogida & Etgen, 1993). The
146 efforts have been made to incorporate these factors into GMPEs (Abrahamson et al., 2014;
147 Campbell & Bozorgnia, 2014; Chiou & Youngs, 2014; Marafi et al., 2017), however, the
148 extensive information required to accurately characterize such basin-specific amplification
149 remains a challenge.

150 As a result, the potential for high cost-benefit risk reduction that would accrue from high-
151 resolution understanding of ground motion variability remains elusive. Typically, GMMs
152 developed in data-rich countries of the global north are reconditioned for deployment in areas for
153 which they have no obvious physical validity (Hough et al., 2016; Nath & Thingbaijam, 2011).
154 At best, this leads to poor spatial resolution precluding the detailed site classification that is
155 critical for seismic microzonation studies needed for cost-effective urban planning (Ansal et al.,
156 2010). The development of appropriate techniques for rapid, local, high-resolution seismic
157 hazard assessment is a significant global challenge.

158 In this research, we approach this challenge by using a simplified decomposition of
159 ground motions into parametric relations explaining the regional and local variations in the
160 measured intensity. We demonstrate the usefulness of PB simulations in capturing the primary
161 low frequency (LF), <1Hz, sedimentary basin effects that contribute to the variation in ground
162 motion within an *urban* area situated within a seismically active region. We show, to first order,

163 seismic intensity decays along the wave path according to the integrated rheological properties of
 164 the region and is concurrently subject to relative amplification specific to any point on the
 165 surface. We first provide the theoretical physical basis for the decomposition and then describe
 166 the simulation domain and the numerical scheme used to explore it. We then describe how the
 167 main elements of the problem can be extracted from the simulations and demonstrate the
 168 convergence of the simulated ground motions providing measureable fields (Δ and A , explained
 169 in the subsequent section) that allow the reconstruction of the originally simulated intensities.
 170 We highlight that the assessment of these parameters is not notably influenced by source
 171 characteristics (such as location and directivity). Therefore, calibrating these parameters and
 172 understanding short-scale ground motion amplification variability can address the challenge
 173 posed by the lack of earthquake data. We suggest that this approach, when extended to including
 174 Higher Frequencies (HF), might provide an improved relative seismic risk assessment in the
 175 form of more reliable microzonation maps at the scale of urban planning, which is based on rapid
 176 seismological site characterization in the absence of long duration seismic catalogues.

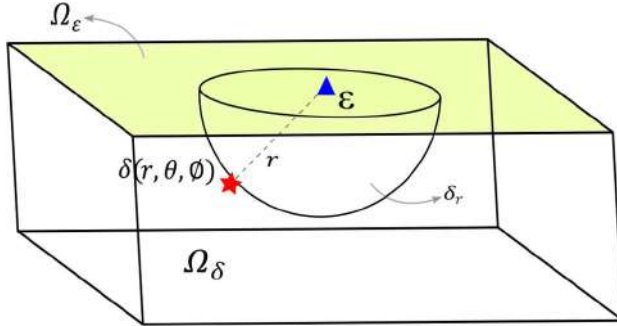
177 **2 Theoretical considerations**

178 Using the seismic representation theorem, (De Hoop, 1958; Knopoff, 1956), in polar coordinates
 179 the displacement $\mathbf{U}_{\delta,\epsilon}$ recorded at a site ϵ for a point-source earthquake δ is given by:

$$180 \quad \mathbf{U}_{\delta,\epsilon} = \mathbf{G}_{\delta(r,\theta,\phi),\epsilon} * \mathbf{f}_{\delta(r,\theta,\phi)} \quad (2)$$

181 Where, r is the distance between source and receiver, and θ and ϕ are the positional angles in a
 182 spherical coordinate system, \mathbf{f}_{δ} is a force vector at δ and \mathbf{G} is the elastodynamic Green's

183 function providing the displacement at $\boldsymbol{\varepsilon}$ due to \boldsymbol{f}_δ . Since we consider the peak displacement
 184 rather than a displacement time series in what follows, this equation is time invariant.



185
 186 *Figure 1: A cuboidal domain having a receiver at $\boldsymbol{\varepsilon}$ and a seismic point source at $\boldsymbol{\delta}(r, \theta, \phi)$. The*
 187 *top surface of this domain represents receiver field Ω_ε and the volume defines a source field Ω_δ .*
 188 *All sources at a distance r from $\boldsymbol{\varepsilon}$ can be represented as the surface of hemisphere δ_r . These*
 189 *ground motion intensity at $\boldsymbol{\varepsilon}$ due to these sources are integrated in equation 3. This can further*
 190 *be integrated for all receivers at the surface Ω_ε , as calculated in equation 4.*

191 Consider a receiver at point $\boldsymbol{\varepsilon}$ that experiences displacements due to sources of a given seismic
 192 moment at a point $\boldsymbol{\delta}$ (see Figure 1). The average logarithm of the peak displacement field for all
 193 possible point sources $\boldsymbol{\delta}_r$ at distance r from the receiver $\boldsymbol{\varepsilon}$ can then be expressed as-

$$194 \quad \overline{\ln(U_{\delta_r, \boldsymbol{\varepsilon}})} = \frac{1}{2\pi^2} \int_0^\pi \int_0^{2\pi} \ln(U_{\boldsymbol{\delta}(r, \theta, \phi), \boldsymbol{\varepsilon}}) d\theta d\phi \quad (3)$$

195 $\overline{\ln(U_{\delta_r, \boldsymbol{\varepsilon}})}$ then represents the expectation value for the intensity at $\boldsymbol{\varepsilon}$ due to all possible events at
 196 distance r . In this formulation, we consider point sources without any particular focal
 197 mechanism, so equation 3 might be considered as an integration over all possible focal
 198 mechanisms at all possible points on the hemisphere.

199 Integrating over all receivers Ω_ε on the surface of the domain:

$$200 \quad \overline{\ln(U_{(\delta\varepsilon)_r})} = \frac{1}{\Omega_\varepsilon} \iint_{\Omega_\varepsilon} \overline{\ln(U_{\delta_r, \boldsymbol{\varepsilon}})} d\boldsymbol{\varepsilon} \quad (4)$$

201

202 then provides a mean field estimate of the expected intensity for any source-receiver pair
 203 separated by the distance \mathbf{r} , and a graph of $\overline{\ln(\mathbf{U}_{(\delta\epsilon)_r})}$ against \mathbf{r} , represents the mean field decay
 204 of intensity with distance throughout the entire volume.

205 The response at a particular location on the surface to any specific event at some distance \mathbf{r} will,
 206 of course, be subject to the source, path and site effects, all contributing to some local
 207 modification of the mean field expectation. Consider the ground motion at a receiver ϵ due to
 208 any source δ , again, the peak displacement ($\mathbf{U}_{\delta,\epsilon}$) can be calculated using the representation
 209 theorem, this time giving:

$$210 \quad \mathbf{U}_{\delta,\epsilon} = \mathbf{G}_{\delta,\epsilon} * \mathbf{f}_{\delta} \quad (5)$$

211 This peak ground displacement $\mathbf{U}_{\delta,\epsilon}$ varies with ϵ but from Equation 4, we know its mean across
 212 the surface is $\overline{\ln(\mathbf{U}_{(\delta\epsilon)_r})}$. Normalising the $\mathbf{U}_{\delta,\epsilon}$ by $\overline{\ln(\mathbf{U}_{(\delta\epsilon)_r})}$ removes the mean field decay
 213 leading to a normalised displacement $\widehat{\mathbf{U}}_{\delta,\epsilon}$ given by:

$$214 \quad \widehat{\mathbf{U}}_{\delta,\epsilon} = \frac{\mathbf{U}_{\delta,\epsilon}}{\overline{\ln(\mathbf{U}_{(\delta\epsilon)_r})}} \quad (6)$$

215 Finally, to encapsulate the effect of all possible sources at each receiver, this normalised
 216 displacement can be integrated for the entire source field (Ω_{δ}),
 217 giving:

$$218 \quad \overline{\ln(\widehat{\mathbf{U}}_{\epsilon})} = \frac{1}{\Omega_{\delta}} \iiint_{\Omega_{\delta}} \ln(\widehat{\mathbf{U}}_{\delta,\epsilon}) \, d\delta \quad (7)$$

219 This $\overline{\ln(\widehat{\mathbf{U}}_{\epsilon})}$ describes a local normalised amplification expected at any point for all possible
 220 sources. This can be considered as the integrated effect of the whole wave path from all possible
 221 sources that is dominated near ϵ where these paths converge. This term introduces the empirical
 222 site-specific variability using the normalised intensity of a suite of earthquakes of any magnitude.

223 Equations 4 and 7 now allow us to express the final estimate of intensity measure as:

$$224 \quad \ln(IM) = \overline{\ln(\mathbf{U}_{(\delta\epsilon)_r})} + \overline{\ln(\widehat{\mathbf{U}}_{\epsilon})} \quad (8)$$

225 For the sake of simplicity, for an event at i , observed at a location \mathbf{j} , separated by a distance \mathbf{r} ,
 226 $\ln\Delta_r$ is used to denote the first term, the mean intensity decay $\overline{\ln(U_{(\delta\varepsilon)_r})}$ and $\ln A_j$ defines the
 227 second term describing amplification, $\overline{\ln(\bar{U}_\varepsilon)}$. Now, equation 8 can then be re-written as:

$$228 \quad \mathbf{IM}_{ij} = \Delta_r \times A_j \quad (9)$$

229 Where \mathbf{IM}_{ij} is a non-specific intensity measure recognising that the argument so far may be
 230 generalised to peak velocity or acceleration. \mathbf{IM}_{ij} then, provides an estimate of the intensity of
 231 ground motion based on the mean field expected intensity at a distance Δ_r , integrated over the
 232 entire crustal volume under consideration, and a relative amplification A_j due to the integrated
 233 effect of the seismic velocity structure around the site. Both terms on the right hand side are
 234 properties of the crust, regionally and locally, and do not include extended descriptions of the
 235 earthquake source, as we show in the next section. Equation 9 defines the $\Delta - A$ decomposition,
 236 a static ground motion model that emphasises local geology rather than the descriptions of the
 237 earthquake source.

238 In practice, the mean field Δ and amplification A , can both be calibrated through simulation
 239 based estimates for a given domain, hence the basis is essentially non-ergodic, but it is different
 240 than data-based statistically estimated parameters used in typical non-ergodic GMM (e.g.
 241 Landwehr *et al.*, 2016; Kuehn, Abrahamson and Walling, 2019). The spatial coefficients
 242 estimated in these non-ergodic model are data-dependent, hence in order to find potential drivers
 243 of GM variability in data sparse regions, there is very little scope to use these models. To clarify,
 244 the motivation for the potential utility of Δ - A method is to target the data-sparse regions without
 245 extensive availability of earthquake catalogues.

246 **3 Defining Domain and source scenarios for simulations**

247 To explore the behavior and stability of Δ and A (in equation 9) and how they might be estimated
 248 in practice, we use a virtual world that allows the exploration of the ideas in the absence of
 249 uncertainty but which allows the introduction of precisely constrained variability. We use a
 250 virtual crustal environment, as shown in Figure 2 (a,b), that incorporates a simplified subsurface
 251 velocity structure centered on a shallow and a deep river basin overlying a crystalline basement

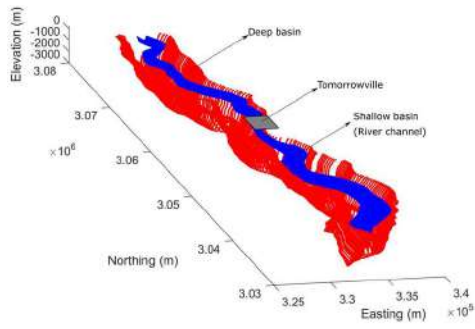
252 to which simplified velocities have been assigned. The description of the domain includes depth
253 varying density (ρ), shear wave speed (V_s), primary wave speed (V_p), and anelastic
254 attenuation factors (Q_p, Q_s), and is determined based on the assumed values of these parameters
255 at the surface of the shallow basin (river channel), deep basin and basement (Brocher, 2005,
256 2008). The reader is referred to the Jenkins *et al.*, 2023, section 3.1 for detailed description for
257 crustal domain and earthquake moment distribution. Alternatively, this information is also
258 accessible in the supplementary materials (Table S1 and Figure S1).

259 In the middle of crustal domain, we locate a virtual urban environment Tomorrowville (Cremen
260 *et al.*, 2023; Gentile *et al.*, 2022; Jenkins *et al.*, 2023; Menteşe *et al.*, 2023; C. Wang *et al.*, 2023).
261 The geology of Tomorrowville is based on a stretch of the Nakhu river valley on the outskirts of
262 Lalitpur to the south of Kathmandu though the velocity structure described here extends far to
263 the north and south, and does not represent the actual subsurface seismic velocity in the area.
264 Instead, we simply generate a hypothetical near-surface velocity structure representative of any
265 urban settlement located around a river channel set in a deeper and wider sedimentary basin. The
266 depths of shallow and deep basins in Tomorrowville are presented in Figure 2 (c,d).

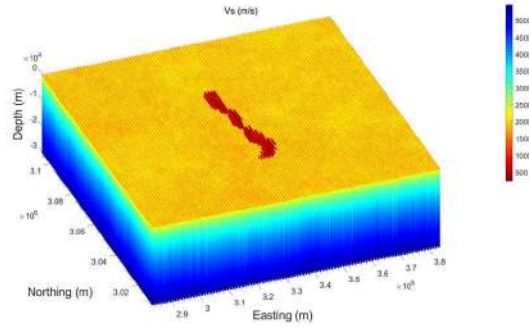
267 The random distribution of 40 events (EQ1 to EQ20 are **Mw6** and EQ21 to EQ40 are **Mw5**) is
268 simulated across the domain (see Figure 2 e,f) using an established physics based solver,
269 SPEED. (Mazzieri, Stupazzini, Guidotti, & Smerzini, 2013; Paolucci *et al.*, 2014; Smerzini *et al.*,
270 2011). Kinematic characterisation of rupture model is done based on the model developed by Liu
271 *et al.*, 2006; Schmedes *et al.*, 2013 in which the correlation between the slip, rise time, peak time
272 and rupture velocity among the sub-faults are derived based on a large ensemble of dynamic
273 rupture simulations of dipping faults. The moment distribution remains same for each magnitude
274 ensemble, but the strike and dip are varied. This distribution of rupture scenarios produce a wide
275 range of expected source directivity for any location. The Peak Ground Acceleration (PGA)
276 maps shown in Figure S2 and Movie S4, are referred for the visualisation of source orientation
277 and their corresponding effects across the surface of entire domain. The wavefront evolution for
278 EQ1 can also be found in Movies S1, S2 and S3 of the supplementary information as well.

279 The Δ - A decomposition, developed theoretically above (Section 2), includes no source
280 variability whereas any attempt to understand seismic hazard must. The azimuth of the events

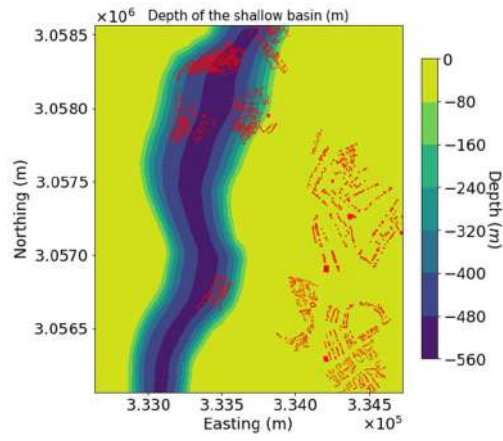
281 from the seismometer with respect to the dominant velocity anisotropy introduced by the river
282 basin will also contribute to the expected ground motion variability. The aim of this manuscript
283 is not to examine the influence of these features on the observed local intensity; that will follow
284 in a later work. Instead, we simply explore the extent to which the relative amplification term,
285 A_j , might act as a usable proxy that, to first order, governs the intensity variation across an urban
286 area, irrespective of the source orientation. This might be considered as a lower bound on the
287 skill of equation 9 in providing the basis for a static site-dependent ground motion model that
288 might be improved later by the introduction of a source term to be constrained by the structural
289 fabric and stress state around any specific location.



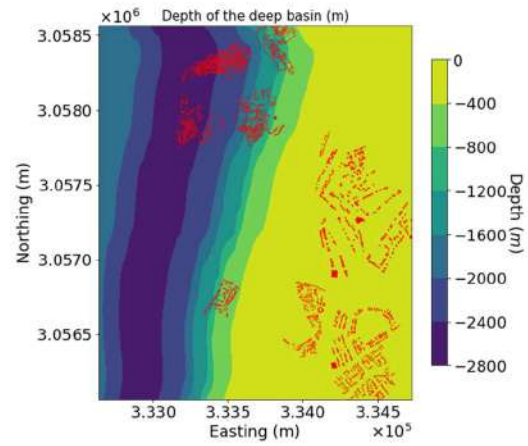
a)



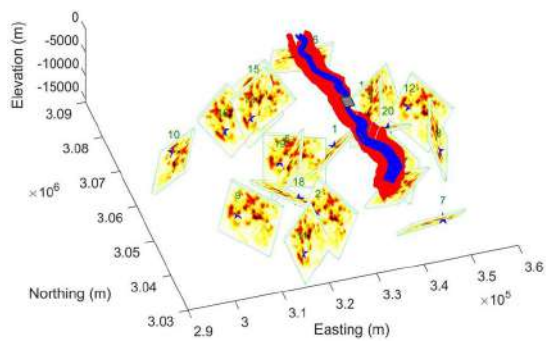
b)



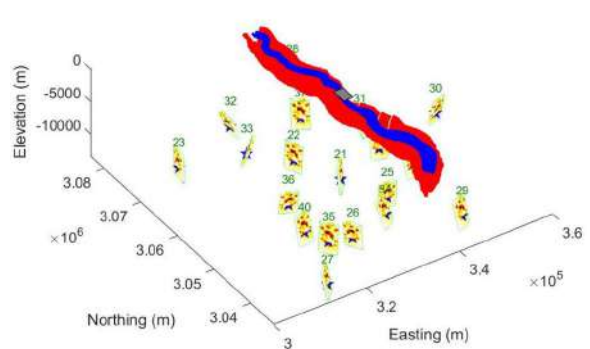
(c)



d)



(e)



(f)

291 *Figure 2: The computational domain used for the simulations and the distribution of earthquake*
 292 *scenarios is shown. a) The sedimentary basin structure showing a river channel creating a*
 293 *shallow basin of maximum depth 500m located inside a 2km deep basin (see Jenkins et al., 2023*
 294 *for details). The gray rectangle represents Tomorrowville (eg. Cremen et al., 2022, Mentese et*
 295 *al., 2022), which has been designed to help understand the implications of development decision*
 296 *making on consequent risk to future communities. b) Represents the extent of the basin*
 297 *geometries using the shear wave velocities in a crustal volume of dimensions 100 km in length,*
 298 *100km in width and 30km in depth. c) and d) show the basin depths of shallow and deep basins*
 299 *across Tomorrowville with buildings distribution (red polygons). The building distribution is*
 300 *shown to highlight the direct impact of seismicity across the potential future infrastructure. e)*
 301 *and f) show 40 thrust earthquakes with random distributions of dip, rake and strike with EQ1 to*
 302 *EQ20 of Mw6 and EQ21 to EQ40 of Mw5 are generated across the domain. The hypocentres*
 303 *are represented by blue stars on the fault surface. The colour distribution across each rupture*
 304 *surface shows the moment release following the kinematic rupture models as developed by Liu et*
 305 *al., 2006; Schmedes et al., 2013.*

306 **4 Estimation of Δ and A for Tomorrowville**

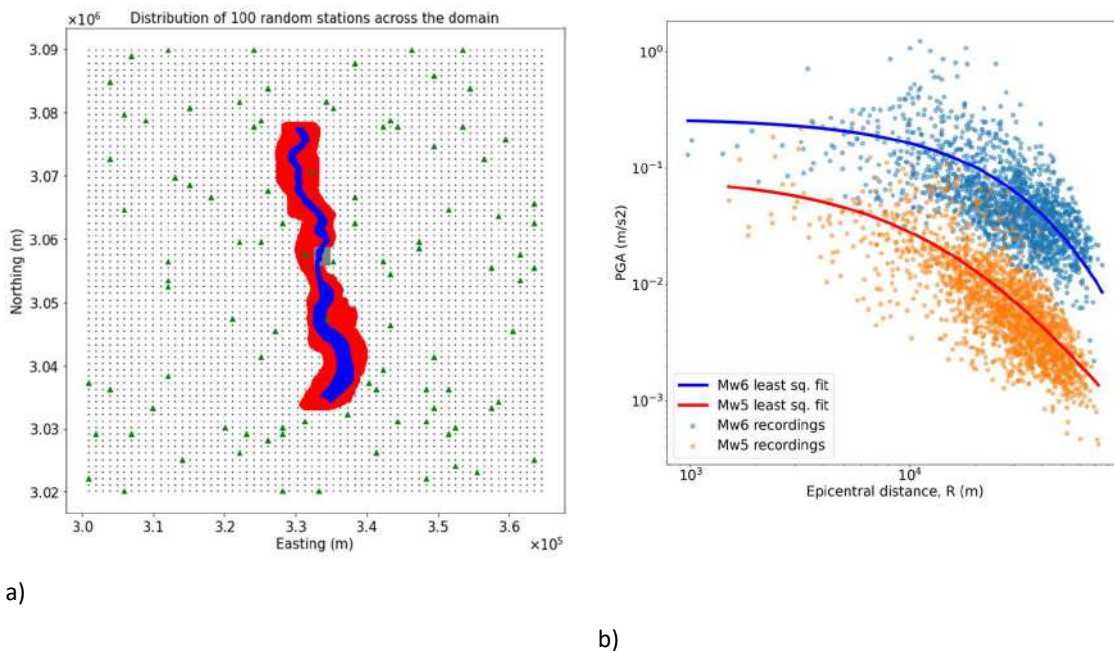
307 The simulation results are used to estimate the Δ for the crustal domain and A for Tomorrowville
 308 (equation 9). The geometric mean of horizontal components of PGA values are used as intensity
 309 measure for all of the rupture scenarios. The crustal domain has a minimum shear wave velocity
 310 of 250 m/s and the smallest element size of 200m with the spectral degree of 4, hence, the
 311 simulations are able to resolve for the vibrational periods greater than 0.8s.

312 In the entire simulation domain, a random set of 100 recording locations is chosen (see green
 313 triangles in Figure 3a) for which estimates of the PGA are simulated for every event, generating
 314 a large number of estimates of the peak amplitude for different epicentral distances giving the
 315 data points for magnitude 5 and 6 events shown in figure 3b. We use simple least squares
 316 regression to the decay equation:

$$317 \quad |\Delta_r| = \mathbf{a} + \mathbf{b} \times \ln(\mathbf{r} + \mathbf{c}) \quad (10)$$

318 here, Δ_r is an estimation of the mean field intensity measure Δ_r (introduced in equation 9), \mathbf{r} is
 319 the epicentral distance and a, b and c are the empirical parameters evaluated from the data fitting

320 procedure which might be modified without loss of insight (Figure 3b). It should be noted that
 321 the regression method chosen here does not distinguish the repeatable (within event) and non-
 322 repeatable (between event) effects, which is followed from the fact that each source used here is
 323 characteristically similar and is recorded at the exact same set of receivers. Assuming the entire
 324 domain has a homogeneous earthquake distribution, each recording is considered independent,
 325 irrespective of whether the seismic energy is originated from same or different sources. The
 326 concept of earthquake source homogeneity implies that in a scenario with limited prior
 327 knowledge of the tectonics in the area, a reverse faulting earthquake could potentially occur at
 328 any azimuth with respect to the city.



329 *Figure 3: a) A map of the computational domain showing the shallow basin (blue) created by*
 330 *river channel, and a deep basin (red), as well as the location of Tomorrowville (gray). Green*
 331 *triangles indicate the random locations of the 100 virtual seismometers. b) points indicate PGA*
 332 *versus epicentral distance for each of the 40 events at each virtual seismometer and the curves*
 333 *represents the least squares estimate of the mean field amplitude decay for this data.*

334 We now must turn our attention to the variability of the data around the curves (Figure 3b) and
 335 will focus on the Tomorrowville sub-domain. Note, any numerical uncertainties due to the
 336 calculation, conditional on the input geological structure, are negligible compared to the

337 variability observed in figure 3b. Hence, given the assumption that the simulation is providing
338 accurate estimates in a virtual setting, each point in figure 3b accurately represents the local peak
339 amplitude of waves from a particular event recorded at a single station. To estimate $|A_j|$ for any
340 location j , the PGA values from all events are extracted for the Tomorrowville domain (Figure
341 4c).

342 As an example, PGA from earthquake 1 (EQ1) is shown along with the spectral accelerations
343 (5% damped) at 10 stations, S1 to S10 (Figure 4 a,b). It can be clearly seen that the basin area is
344 showing strong amplification resulting in higher PGA values due to wave trapping and resonance
345 of the sedimentary basin layers, as compared to the lower PGA values along the areas of
346 crystalline basement. Spectral accelerations at 10 stations show different orders of amplification
347 over the entire period range (0.8s to 5s) corresponding to the geological locations of these
348 stations. The consistent decrease in amplitude with increasing period observed at all stations
349 indicates that it is majorly controlled by the selected source spectra. Stations S2, S3 and S7 lie in
350 the combined (both deep and shallow) basin area and hence, recording maximum amplification,
351 while the stations S1 and S6 lie above only deep basin area, hence the amplification is lesser but
352 still significant at higher periods for all three components. The rest of the stations, S4, S5, S9 and
353 S10 are situated over the basement rocks, hence recording the lowest value of spectral
354 accelerations.

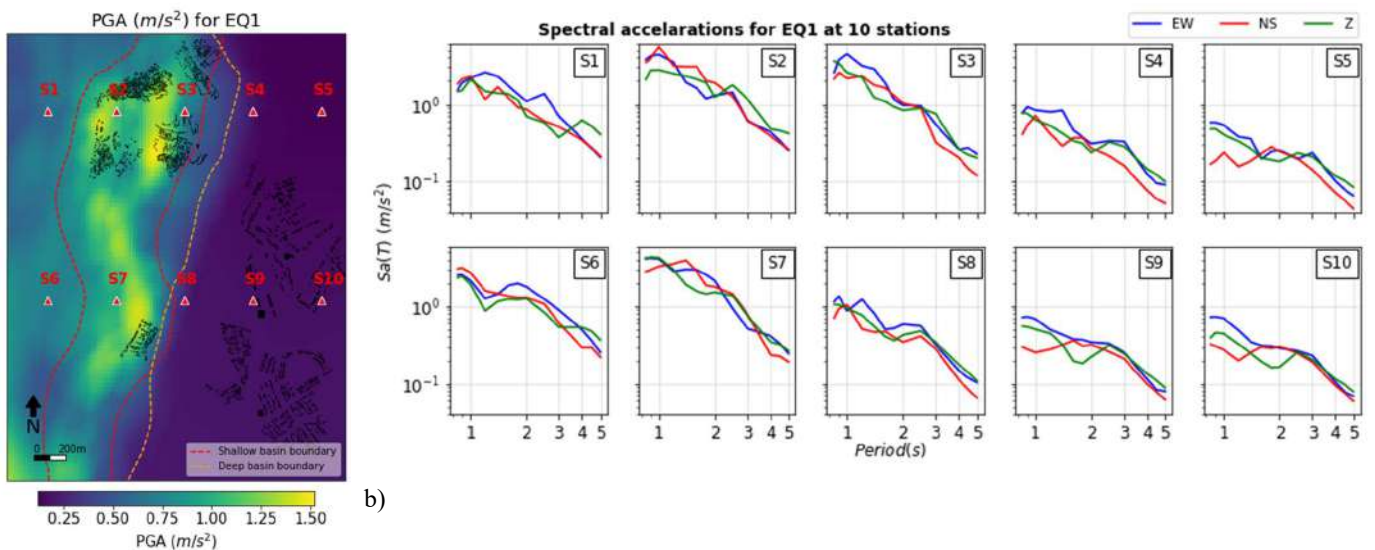
355 Our simulations focus on frequencies below 1Hz due to high computational costs associated with
356 sampling higher frequencies. However, this analysis remains relevant since basins, like the
357 Kathmandu basin, often exhibit resonance at similar frequencies (Asimaki et al., 2017; Oral et
358 al., 2022). Additionally, when dealing with higher frequencies, it becomes necessary to account
359 for other non-linear site effects that play a significant role in intensity variations (Semblat et al.,
360 2005), which are not included in this analysis.

361 Given the geometry of the basin stretched approximately North-South (NS) whilst being much
362 more confined along East-West (EW), the amplification of both horizontal components should
363 be theoretically contrasting. However, the periods resolved in the simulations suggest the inter-
364 component variability is still lower than the inter-station variability across different geological

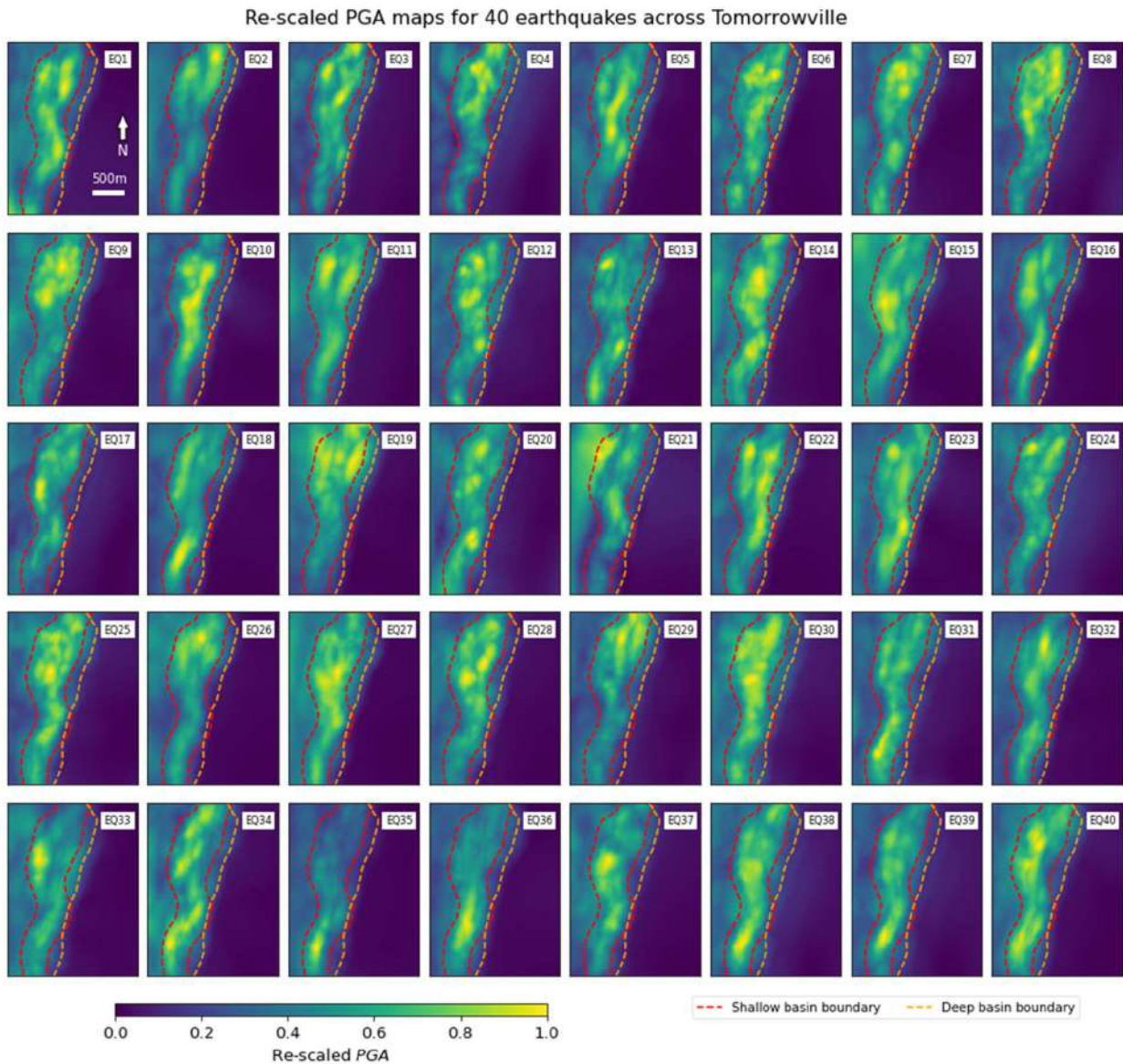
365 domains (Figure 4b). This suggests, the geometric mean of the horizontal components of PGA at
 366 each station seem a usable guide to explore the amplification further discussed in this study.

367 The pattern of higher amplification along the river basin and lower amplification along the
 368 basement area is common for PGA maps of all the earthquake scenarios (Figure 4c). Hence
 369 while the absolute PGA is strongly dependent on the source magnitude and distance, the *relative*
 370 amplitude within any map is qualitatively independent of earthquake source orientation, and
 371 even magnitude. The structural similarity of PGA maps in Figure 4c seems to indicate the
 372 potential utility of the Δ -*A* decomposition.

373



a)



c)

374 *Figure 4: Simulation results are extracted for Tomorrowville domain. a) Shows the PGA*
 375 *(geometric mean of two horizontal components) values for EQ1 along with the boundaries of*
 376 *shallow and deep basins, represented by red and orange dashed lines, respectively. Red triangles*
 377 *show 10 stations, S1 to S10 that are used to show the spectral accelerations for the 0.8s to 5s in*
 378 *b). Three components East-West (EW), North-South (NS) and Vertical (Z) are plotted separately.*
 379 *c) PGA maps for 40 events plotted on TV city domain. EQ1 to EQ20 represent data from Mw6*
 380 *earthquakes while EQ21 to EQ40 are for Mw5. Note that we have scaled each map between 0*
 381 *and 1, where 0 is minimum and 1 is maximum PGA for each earthquake. The similarity of the*

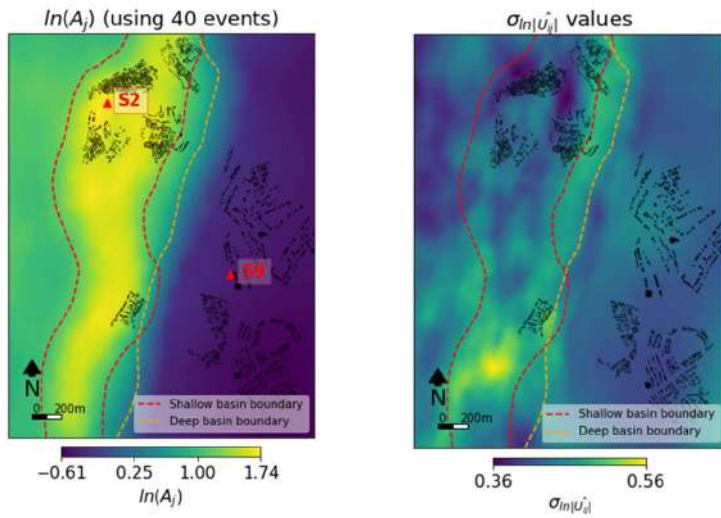
382 *maps indicates that, to first order, regardless of the absolute value of the PGA across the zone,*
 383 *the relative amplitude for different locations is invariant.*

384 To extract this pervasive feature of relative amplification from all earthquake scenarios we
 385 normalise and stack the PGA maps for each event. First, all PGA maps are normalised using the
 386 mean smooth earth expectation value $|\Delta_r|$, calculated from equation 10. This normalisation is the
 387 practical implementation from the theoretical description given in the equation 6, where the
 388 normalisation factor is taken as the mean intensity decay in equation 4. Let, $|U_{ij}|$ be the
 389 simulated PGA at a particular site j due to an earthquake i at a distance r , then the normalised
 390 PGA $|\widehat{U}_{ij}|$ would be –

$$391 \quad |\widehat{U}_{ij}| = |U_{ij}| / |\Delta_r| \quad (11)$$

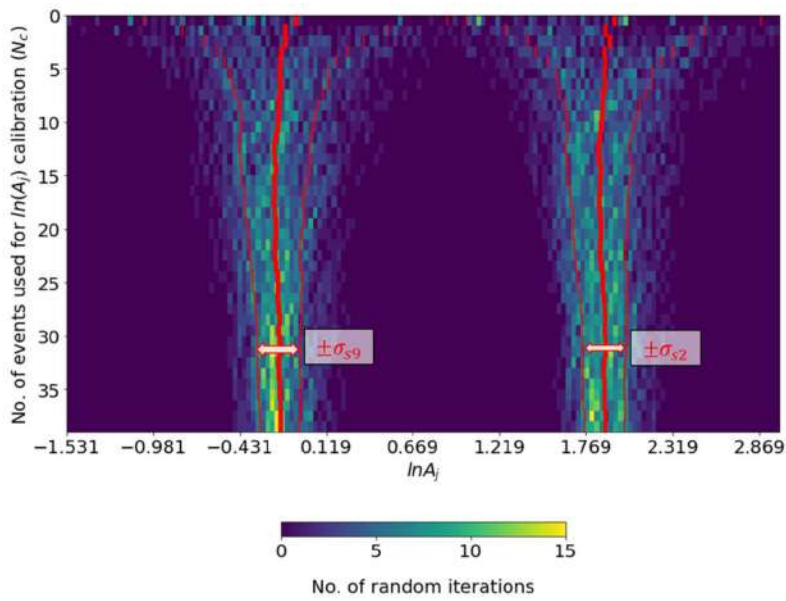
392 After normalisation, the average PGA of the normalised maps is calculated for N_e number of
 393 earthquake scenarios, as described in equation 7. This final, averaged PGA map is a
 394 characteristic spatial kernel for the chosen city domain and theoretically contains the average
 395 local amplification (A_j) at any site j for any possible earthquake regardless of source, (see Figure
 396 5a). Here, A_j has the following form-

$$397 \quad A_j = \left(\prod_{i=1}^{N_e} |\widehat{U}_{ij}| \right)^{\frac{1}{N_e}} \quad (12)$$



a)

b)



c)

398 *Figure 5: a) Estimates of $\ln A_j$, and b) the standard deviation ($\sigma_{\ln|\widehat{U}_j|}$) for Tomorrowville. Two*
 399 *locations, one in the river basin (S2), and one where the crystalline basement outcrops at the*
 400 *surface at (S9) are chosen in a), to plot the convergence of the $\ln A_j$ at S2 and S9 with an*
 401 *increasing number of events as shown in c).*

402 The calculation of A_j results in a mean amplification field consistent with the spatial variations
 403 observed in the simulations (Figure 5a). Each pixel represents the mean amplification
 404 experienced at that location over all magnitudes, azimuths and directivity.

405 There is, of course, a dispersion of $\ln[\widehat{U}_y]$ values around this mean which is itself a spatially
 406 variable field over the domain, calculated by the $\sigma_{\ln[\widehat{U}_y]}$ (Figure 5b) as:

$$407 \quad \sigma_{\ln[\widehat{U}_y]} = \sqrt{\frac{1}{N_e} \sum_{i=1}^{N_e} (\ln[\widehat{U}_y] - \ln A_j)^2} \quad (13)$$

408 where, $\sigma_{\ln[\widehat{U}_y]}$ gives the variability due to various source scenarios used in the analysis and the
 409 corresponding path effects. The maximum value of $\sigma_{\ln[\widehat{U}_y]}$ is 0.56, that is 23.8% of the entire
 410 $\ln A_j$ range of 2.35 in Tomorrowville. The difference of 2.35 in maximum ($\ln A_{j,max}$) and
 411 minimum ($\ln A_{j,min}$) values would mean, the ratio $A_{j,max}/A_{j,min}$ is $e^{2.35} \sim 10.48$, implying an
 412 order of magnitude variation within Tomorrowville. Notably, the ranges of the amplification and
 413 standard deviations are of a realistic order often found in some of the extensively studied real-
 414 world settings as well, for example as shown by Day et al., 2019 in Southern California.

415 Another approach to understanding the variability of the amplification field involves varying the
 416 number of events used to calculate $\ln A_j$ and examining its variability at a specific location using
 417 the events selected through a bootstrapping approach. We chose two stations from Figure 4a, one
 418 representing an area of high amplification over the river basin, named as **S2**, and one in low
 419 amplification over outcropping basement, named as **S9** (see Figure 5a). The number of events
 420 N_c , used to estimate A_j , is plotted against the $\ln A_j$, where the colour intensity represents the
 421 distribution of the iterations across the entire $\ln A_j$ range (Figure 5c). For each N_c value, 100
 422 random combination of events with repetition are used for $\ln A_j$ calculation. The red dashes
 423 correspond to the $\pm 1 \sigma_{s2}$ and $\pm 1 \sigma_{s9}$ variability around the mean $\ln A_j$ value for the respective
 424 N_c value. The convergence of the $\ln A_j$ values can be observed even with as low as ~ 7 events
 425 with a stable $\pm \sigma_{s2}$ and $\pm \sigma_{s9}$ around the $\ln A_j$ values of 0.12 each. This distribution of $\ln A_j$ is

426 non-overlapping for both sites, **S2** and , which suggests that the local crustal features at both of
 427 these sites is the dominant contributor in the amplification.

428 **5 Estimation of PGA using Δ and A for 40 earthquakes**

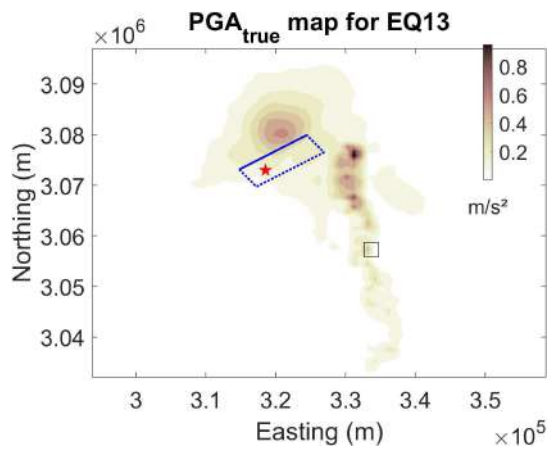
429 The theoretical treatment described in section 2 above suggests that the ground motion at a point
 430 can be decomposed into the effect of the mean field attenuation over the wave path integrated
 431 over the crustal volume and the effect of the local velocity structure. This implies that the
 432 reversal of this process should reproduce the original PGA field. Thus if we have robust
 433 estimates of Δ and A , then we should be able to reproduce the intensity at any point using
 434 equation 9.

435 We demonstrate this process for a single earthquake, EQ13 located 30.4 km to the NW of
 436 Tomorrowville, we will show that the choice of the earthquake is not important. The simulated
 437 PGA at every point will be referred to as the true value, PGA_{true} (see Figure 6a,e). To estimate
 438 the PGA value explained in equation 9 for this event, referred herein as $PGA_{\Delta A}$, we first calibrate
 439 the Δ (Figure 6b) and A (Figure 6c) using the rest of 39 simulated events. Δ and A are multiplied
 440 as shown in equation 9 to obtain $PGA_{\Delta A}$ values for this earthquake (see Figure 6d). A graph of
 441 $PGA_{\Delta A}$ as a function of PGA_{true} is shown in figure 6g along with the histograms of all the grid
 442 points across Tomorrowville. There is a systematic overestimation of $PGA_{\Delta A}$ values for this
 443 particular event at the lower PGA range, and a minor underestimation can be seen at the higher
 444 PGA side. This pattern can be attributed to the characteristic that the $\ln A_j$ values, which are used
 445 to calculate $PGA_{\Delta A}$, have mean amplification values spanning a wider range compared to this
 446 specific event. Pearson correlation coefficient (γ) between logarithms of $PGA_{\Delta A}$ and PGA_{true} is
 447 0.98, suggesting strong correlation between the two. The histograms presented in parallel to the
 448 axes also indicate that the distribution nature of Peak Ground Acceleration (PGA) remains
 449 preserved across Tomorrowville, exhibiting a tri-modal pattern in both PGA_{true} and $PGA_{\Delta A}$
 450 (Figure 6g). This tri-modal pattern is a distinctive influence of three geological domains in the

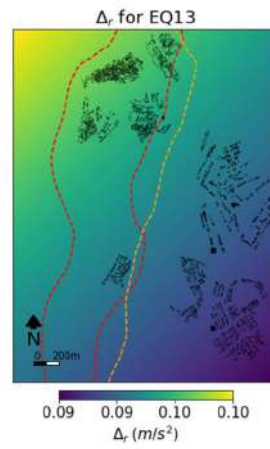
451 city- the deep basin area (to the left of shallow basin boundary), the area comprising both deep
452 and shallow basins, and the basement region.

453 Finally, For each event in the suite of 40 earthquakes, the remaining 39 simulations are used to
454 calculate the Δ and \mathbf{A} , that are multiplied to obtain $PGA_{\Delta A}$. The results are compared with the
455 corresponding PGA_{true} of each earthquake using the γ value and best fitting regression line
456 (Figure 7a). Lowest γ value is 0.89, which suggests the correlation is strong for all the
457 earthquakes. In conclusion, there is a clear potential of predictability in $PGA_{\Delta A}$, with some
458 variability translated from different source-specific variability due to heterogeneous moment
459 distribution along the fault surface, as well as, path related variability due to azimuth of sources
460 with respect to the Tomorrowville. This variability in $PGA_{\Delta A}$, is captured earlier using the
461 $\sigma_{\ln|\widehat{U}_y|}$ values calculated in figure 5b.

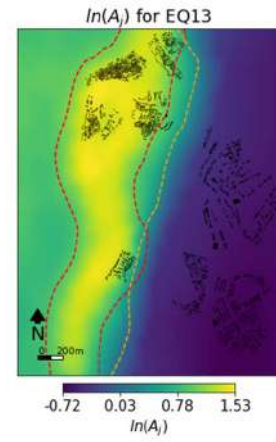
462 The impact of source orientation on the obtained γ value is illustrated by examining three
463 parameters: epicentral distance, back azimuth of the earthquake (bearing of the line joining
464 hypocenter to the center of Tomorrowville), and the angle of approach (the azimuthal difference
465 between the line connecting the hypocenter to the major fault asperity, and the line connecting
466 the hypocenter to the center of Tomorrowville) (Figure 7b). The back-azimuth and angle of
467 approach provide insights into the influence of horizontally anisotropic crustal domain and
468 directivity effects resulting from variations in fault orientation relative to Tomorrowville,
469 respectively. γ is observed to have a positive trend with the epicentral distance indicating that the
470 the earthquakes closer to tomorrowville are poorly constrained by $PGA_{\Delta A}$ compared to the ones
471 farther away. It can also be seen that the chosen earthquake distribution samples a wide range of
472 back-azimuth and angle of approach values, indicating a comprehensive representation of these
473 factors. γ does not show any notable trend with the these two factors, hence, their impact on
474 estimating the distribution of PGA values across Tomorrowville is not substantial.



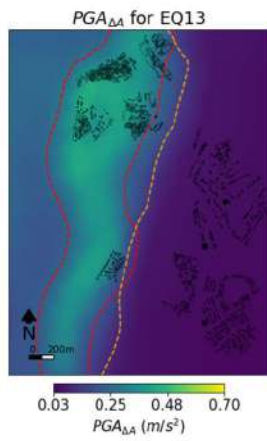
a)



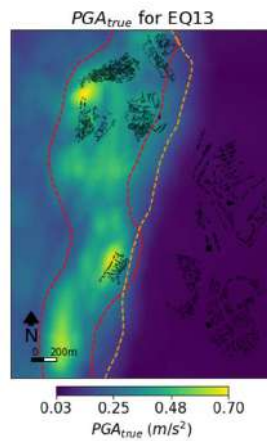
b)



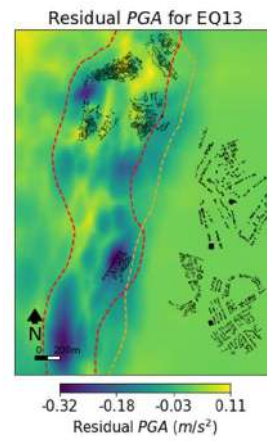
c)



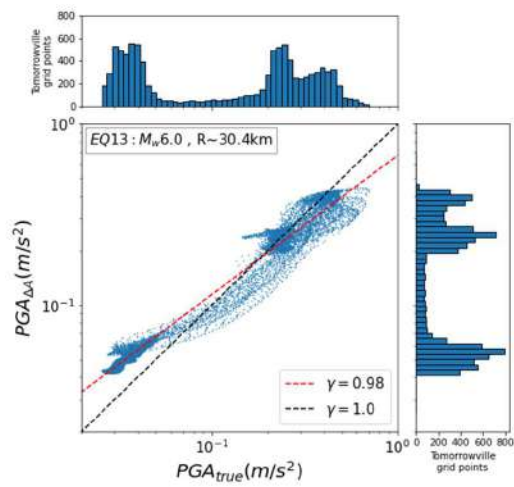
d)



e)

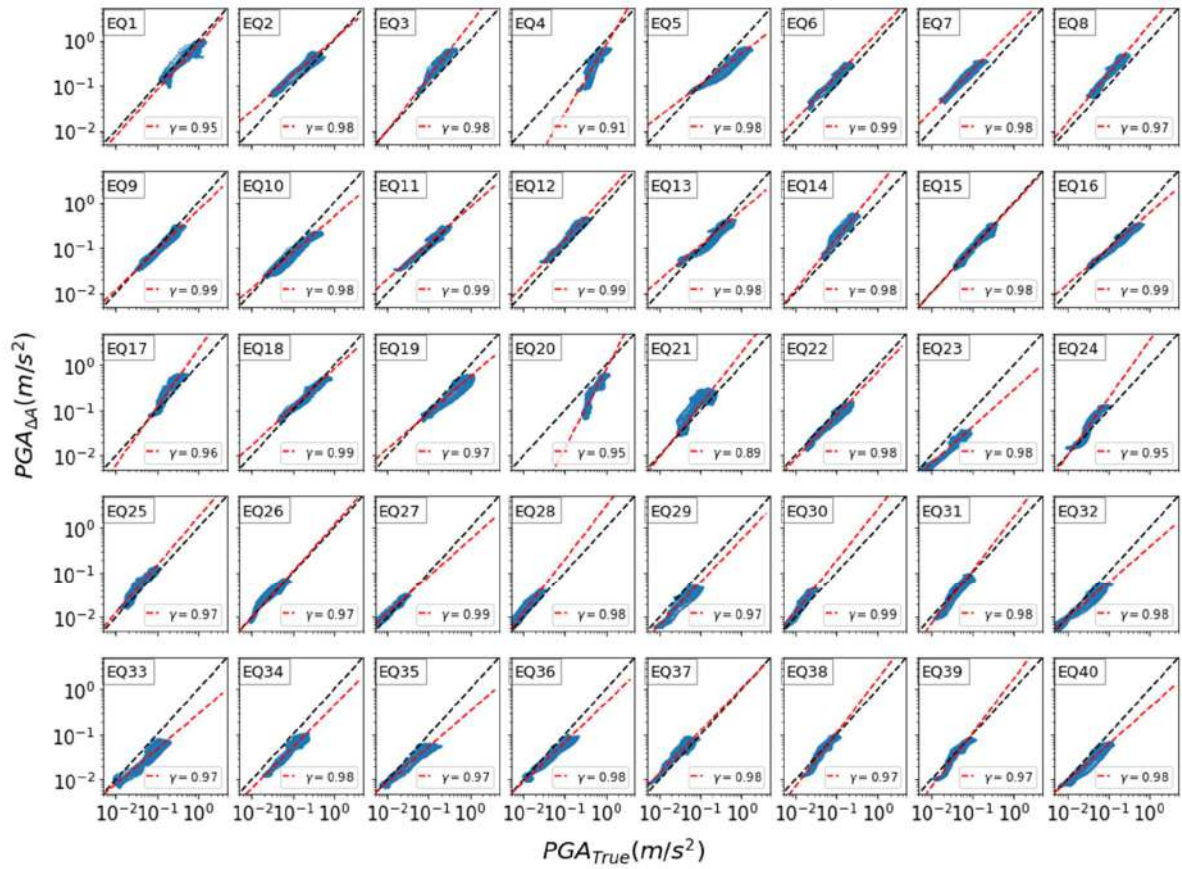


f)

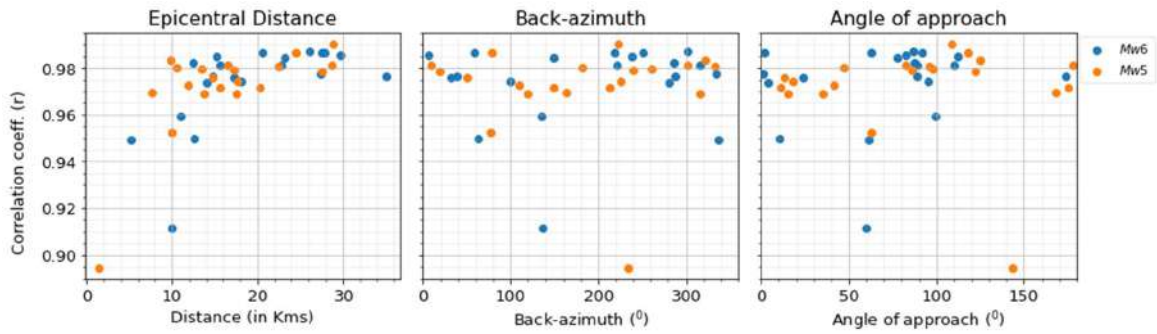


g)

475 *Figure 6: Result showing estimated parameters for EQ13. a) $\mathbf{PGA}_{\text{true}}$ map for EQ13 showing*
476 *the simulation results across the entire crustal domain, the blue dashed-rectangle shows the*
477 *location of rupture surface (top edge is solid blue), red star shows the hypocentre and black*
478 *rectangle in the middle of domain shows the location of Tomorrowville. b) shows Δ_r and c)*
479 *shows $\ln \mathbf{A}_j$ for event EQ13 for Tomorrowville. d) shows the $\mathbf{PGA}_{\Delta A}$ distribution calculated by*
480 *multiplying Δ_r with \mathbf{A}_j as conceptualised in equation 9. e) $\mathbf{PGA}_{\text{true}}$ map for this event obtained*
481 *through the PB simulation. f) residual between $\mathbf{PGA}_{\Delta A}$ and $\mathbf{PGA}_{\text{true}}$ g) shows the comparison*
482 *between $\mathbf{PGA}_{\Delta A}$ and $\mathbf{PGA}_{\text{true}}$ for EQ13 using the Pearson correlation coefficient (γ) of 0.98 for*
483 *this event. Marginal panels show histograms of $\mathbf{PGA}_{\Delta A}$ (right) and $\mathbf{PGA}_{\text{true}}$ (top) indicating the*
484 *similarity in distribution of \mathbf{PGA} values across Tomorrowville city domain.*



a)



b)

485 *Figure 7: $PGA_{\Delta A}$ is calculated for all 40 earthquakes and compared with the simulated PGA*
 486 *values (PGA_{true}). A) Shows the correlation between $PGA_{\Delta A}$ and PGA_{true} for all earthquakes,*

487 *where red dashed line shows the line of best fit and black dashes show the $\gamma = 1$ line. The γ*
488 *value is mentioned for all the earthquakes. B) Shows the γ value versus distribution of the*
489 *following three parameters for all 40 earthquakes- epicentral distance, back-azimuth (bearing of*
490 *line joining hypocenter to the center of Tomorrowville) and angle of approach (the azimuthal*
491 *difference between the line connecting the hypocenter to the major fault asperity, and the line*
492 *connecting the hypocenter to the center of Tomorrowville).*

493 **6 Discussion and summary**

494 Estimates from UNDRR suggest that the number of people at risk from a major earthquake will
495 increase from some 370 million in 2020 to more than 850 million by 2050 (UN-Habitat, 2022).
496 Due to historically unprecedented rapid urbanization, these people will be increasingly
497 concentrated in urban centers; the same source estimates that by 2050 global urban population
498 will increase from the current 56% to around 68% with 95% of this growth happening in the
499 global south. Without a concerted effort at providing decision support for high cost-benefit risk
500 sensitive construction, ongoing urbanization in areas of high seismic hazard, will increase
501 disaster risk for millions.

502 That the intensity of seismic shaking varies at high spatial frequencies is graphically
503 demonstrated by large differences of seismic damage over very short distances in areas of
504 uniform building code (Bielak et al., 1999; see also Asimaki et al., 2012; Dolce et al., 2003;
505 Ohsumi et al., 2016; Sextos et al., 2018). What is less well known is the extent to which this
506 variability is the result of differences in the earthquake source, or in contrasts in the rheological
507 properties of the near surface that might impose a stable and estimable LF amplification, to first
508 order independent of that source. The former prioritizes forecasting likely earthquake sources in
509 seismic hazard assessment, while the latter suggests that measuring the properties of the near
510 surface might produce a pathway to understanding spatial patterns of seismic shaking regardless
511 of the source. This would in turn open a path to the development of physics-based, high-
512 resolution building-code classification and support evidence based seismic urban planning
513 policy.

514 Current methods for seismic hazard assessment require seismic catalogues built from long-term
515 deployment of large numbers of seismometers to calibrate ground motion models (Douglas,

516 2017; Douglas & Aochi, 2008; Douglas & Edwards, 2016a). The observed variability around
517 these models is assumed to be stochastic and statistical methods are used to provide the moments
518 of the emerging distributions leading to low spatial resolution estimates of seismic hazard. Over
519 most of the Global South such long-term data has not been collected nor is there any current
520 appetite for deploying dense networks of seismometers required for this assessment at the
521 resolution which would be required to guide seismic risk informed urban planning at actionable
522 scales.

523 In this study we have harnessed the potential of high resolution PB earthquake simulations to
524 explore the extent to which seismic intensity variability might be described by near-surface
525 geology and that relative seismic intensity is independent of the earthquake source. Do some
526 areas shake more than others, regardless of the earthquake? We exploit the certainty of a virtual
527 world, Tomorrowville, in which the rheology, described by the geometry of the seismic velocity,
528 is known everywhere, in which seismic sources are precisely described by kinematic models
529 (Graves & Pitarka, 2010; Schmedes et al., 2013), and in which wave propagation is perfectly
530 described by the wave propagation solver we use (Mazzieri et al., 2013). In Tomorrowville,
531 dense arrays of ideal seismometers record the wave field across the surface.

532 The study develops a Δ - \mathbf{A} decomposition, that splits the seismic process into a mean-field
533 attenuation model, describing the amplitude decay with source-receiver distance, and an
534 amplification field, describing the integrated amplification of the entire wave path as experienced
535 at each point on the surface. We have shown methods for the estimation of the Δ model and for
536 the \mathbf{A} field for Tomorrowville and demonstrated that their description can be used estimate the
537 true PGA field.

538 This study utilizes PB simulations in a virtual environment that shows a significant fraction of
539 the observed variability can be explained without categorizing them as stochastic. In the real
540 world, beyond these deterministic variations, stochastic elements of the process must be
541 considered separately. Moreover, it becomes important to classify uncertainties as aleatory or
542 epistemic, when the real data guides the model fitting and resulting deviations (Kiureghian &
543 Ditlevsen, 2009). However, in this study, PB simulation results are assumed to be devoid of any
544 modelling uncertainties (or aleatory variability) and they are treated as reproducible true

545 solutions in the analysis. Consequently, the deviations obtained in the results of figure 7A are
546 fundamentally epistemological. The difference between the amplification map for any event and
547 the A field that determines the value of the local PGA, is precisely quantified and accessible.
548 Investigations show that the maximum standard deviation of the A field is about 23.8% of the
549 $\ln A_j$ measured across the entire area, that includes the source and path dependent variability.
550 More importantly, analysis of the variability of the amplification value at any point, indicated
551 stable convergence from as few as 7 event simulations. Furthermore, comparisons of
552 amplifications at locations over the river basin with locations on basement in Tomorrowville,
553 produced stable, order-of-magnitude differences in amplification which converged rapidly and
554 which gave stable non-overlapping amplification estimates. Of course, both the stability and the
555 contrast in amplification are functions of the choice of velocity distribution but the choice of
556 model here was developed to reflect not uncommon velocity geometry not to accentuate
557 amplification contrasts. We expect that the general conclusions of this work are independent of
558 the details of the Tomorrowville velocity model.

559 We have not attempted to explore the variability of the amplification with the source parameters
560 and the initial results suggest that the influence is not likely to be strong. The main candidates,
561 source directivity and epicentral azimuth, expected to be dominant in the strongly anisotropic
562 velocity model used here, do not make an appreciable systematic contribution to the A_j field.
563 Descriptions of active fault geometry and seismotectonics of Tomorrowville could impose a
564 source fabric introducing some systematic influence on the amplification field. Incorporation of
565 any such influence could only constrain the variability so the results described here might be
566 considered as a lower bound on the stability of the A field. The primary factor influencing
567 ground motion amplification in this study is the basin geometry or buried topography, although
568 the impact of surface topography is also anticipated to significantly affect the amplification
569 pattern (García-Pérez et al., 2021; Geli et al., 1988; Lee et al., 2009; Poursartip et al., 2020). The
570 surface topography, often rich in high-resolution data, is the most straightforward to control, and
571 it is expected to contribute to the observed variability. Future research will concentrate on

572 investigating the influence of surface topographic features, in addition to buried topography, on
573 the amplification phenomenon.

574 The reconstruction of the simulated PGA fields provided further evidence of the efficacy of the
575 method. Using estimates of the Δ and \mathbf{A} components from a set of 39 simulations provided strong
576 correlations between true and inverted PGA fields for the 40th. Further, in keeping with the
577 observation of non-overlapping amplification values for basement and basin locations, places
578 with high shaking were broadly consistently high for all events, locations experiencing low
579 intensity shaking were also consistent across all events.

580 The results are suggestive of an underlying physical process in which small-scale LF *relative*
581 shaking intensity is controlled more by local geology than by source process. Thus, given the
582 description of the relevant fields, it is possible in milliseconds of computing time, to estimate the
583 entire PGA field for an event of a given magnitude and location which currently takes days of
584 computation using commonly available computer clusters. At the minimum, this provides a
585 workflow through which normal probabilistic seismic hazard assessments, that require estimates
586 of PGA for thousands of events at each location, can benefit from the advances in physics based
587 simulations without the massive compute overhead that make these computations unfeasible at
588 present.

589 The stability of the relative amplification field together with the stable, order of magnitude
590 difference in PGA across the surface of Tomorrowville demonstrated in this study, points to
591 methods for high-resolution seismic hazard estimation based on understanding the static
592 properties of the near surface, rather than on the unpredictable properties of future earthquakes.
593 The challenge becomes a problem of measurement, rather than forecasting. There remains the
594 critical problem either of the elucidation of the velocity structure of the near surface (Sebastiano
595 et al., 2019), so the Δ and \mathbf{A} fields might be estimated through simulation as in this paper, or the
596 direct estimation of the field by measurement of the intensity of shaking at high resolution in the
597 area of interest. To clarify again, this study explores only LF near-surface effects arising from
598 the presence of complex sedimentary basins and show their contribution in short-scale variability
599 in amplification. It's noteworthy that these LF effects are additional to the site effects related to
600 very-near surface (decameter) depths, which include nonlinear soil responses and other high

601 spatial-frequency velocity variations, all of which can lead to intricate outcomes (Taborda et al.,
602 2012). Consequently, for applications like enhancing microzonation maps, it's imperative to
603 merge this analysis with elements accounting for HF variability.

604 In conclusion, rapid urban expansion in areas of poor historical instrumentation leaves
605 significant gaps in data for seismic hazard assessment. Furthermore, current methods both
606 require decade long deployment of dense seismic networks in the area of near-future urban
607 development and fail to provide high-resolution assessments that identify areas of strong and
608 weak shaking that could underpin high cost-benefit seismic code classification. The potential of
609 physics based simulations has prompted the evaluation of the seismic wave field across areas of
610 near-future development. The results suggest methods to allow the rapid, high-resolution
611 assessment of geological structure that could lead to risk assessment at unprecedented resolution.
612 Contemporary advances in ambient noise tomography techniques that are used for shallow
613 crustal structure determination could make this a realistic approach (Bard et al., 2010).

614 **Acknowledgments**

615 This research is a part of the wider PhD project 'Physics-based Ground Motion Simulations and
616 Uncertainty Assessment in Rapidly Urbanising Environments'. The PhD student is funded by
617 University of Edinburgh, School of Geosciences. This research project is also supported by the
618 Tomorrow Cities Hub (UKRI/GCRF fund under grant NE/S009000/1). Authors thank initial
619 discussions and simulations obtained with the prompt support and guidance from Karim Tarbali,
620 former PDRA at the University of Edinburgh. We thank Gemma Cremen, Chris J. Bean, Mark
621 Naylor and Ian Main for providing constructive feedback and guidance in improving the
622 manuscript.

623 **Open Research**

624 The data used in this research are mainly the simulation outputs, which are extensive in scale.
625 Consequently, we are actively involved in the process of archiving this data. Due to the
626 substantial volume of this dataset, we aim to make it accessible through our institution's data-
627 sharing platform, Edinburgh DATAshare (<https://datashare.ed.ac.uk>). It's important to note that
628 critical information regarding the crustal domain, earthquake hypocenter, and PGA data, which

629 is pivotal for generating the majority of the manuscript's results, can be found in the
630 supplementary material. For more detailed information on earthquake moment distribution, we
631 encourage readers to refer to Jenkins et al. 2023. The software used to run the simulation is an
632 open-source package, SPEED (Mazzieri et al., 2013). The data analysis and processing is done
633 using basic programming language, Python.

634 **References**

- 635 Abrahamson, N. A., Silva, W. J., & Kamai, R. (2014). Summary of the ASK14 ground motion
636 relation for active crustal regions. *Earthquake Spectra*, *30*(3), 1025–1055.
637 <https://doi.org/10.1193/070913EQS198M>
- 638 Aki, K. (1993). Local site effects on weak and strong ground motion. *Tectonophysics*, *218*(1–3),
639 93–111. [https://doi.org/10.1016/0040-1951\(93\)90262-I](https://doi.org/10.1016/0040-1951(93)90262-I)
- 640 Ancheta, T. D., Darragh, R. B., Stewart, J. P., Seyhan, E., Silva, W. J., Chiou, B. S. J., ...
641 Donahue, J. L. (2014). NGA-West2 database. *Earthquake Spectra*, *30*(3), 989–1005.
642 <https://doi.org/10.1193/070913EQS197M>
- 643 Anderson, J. G., & Brune, J. N. (1999). Probabilistic Seismic Hazard Analysis without the
644 Ergodic Assumption. *Seismological Research Letters*, *70*(1), 19–28.
645 <https://doi.org/10.1785/GSSRL.70.1.19>
- 646 Ansal, A., Kurtuluş, A., & Tönük, G. (2010). Seismic microzonation and earthquake damage
647 scenarios for urban areas. *Soil Dynamics and Earthquake Engineering*, *30*(11), 1319–1328.
648 <https://doi.org/10.1016/j.soildyn.2010.06.004>
- 649 Asimaki, D., Ledezma, C., Montalva, G. A., Tassara, A., Mylonakis, G., & Boroschek, R.
650 (2012). Site effects and damage patterns. *Earthquake Spectra*, *28*(S1), S55–S74.
651 <https://doi.org/10.1193/1.4000029>
- 652 Asimaki, D., Mohammadi, K., Mason, H. B., Adams, R. K., Rajaure, S., & Khadka, D. (2017).
653 Observations and Simulations of Basin Effects in the Kathmandu Valley during the 2015
654 Gorkha, Nepal, Earthquake Sequence: *Earthquake Spectra*, *33*(S1), S35–S53.
655 <https://doi.org/10.1193/013117EQS022M>

- 656 Atkinson, G. M., & Boore, D. M. (2006). Earthquake Ground-Motion Prediction Equations for
657 Eastern North America. *Bulletin of the Seismological Society of America*, 96(6), 2181–
658 2205. <https://doi.org/10.1785/0120050245>
- 659 Baker, J. W., Bradley, B. A., & Stafford, P. J. (2021). *Probabilistic seismic hazard and risk*
660 *analysis*. Cambridge University Press.
- 661 Bard, P.-Y., Cadet, H., Endrun, B., Hobiger, M., Renalier, F., Theodulidis, N., ... Kristekova, M.
662 (2010). From Non-invasive Site Characterization to Site Amplification: Recent Advances in
663 the Use of Ambient Vibration Measurements. In M. Garevski & A. Ansal (Eds.),
664 *Earthquake Engineering in Europe* (pp. 105–123). Springer Netherlands.
665 https://doi.org/10.1007/978-90-481-9544-2_5
- 666 Bazzurro, P., & Cornell, C. A. (2004a). Ground-motion amplification in nonlinear soil sites with
667 uncertain properties. *Bulletin of the Seismological Society of America*, 94(6), 2090–2109.
668 <https://doi.org/10.1785/0120030215>
- 669 Bazzurro, P., & Cornell, C. A. (2004b). Nonlinear soil-site effects in probabilistic seismic-hazard
670 analysis. *Bulletin of the Seismological Society of America*, 94(6), 2110–2123.
671 <https://doi.org/10.1785/0120030216>
- 672 Bielak, J., Xu, J., & Ghattas, O. (1999). Earthquake Ground Motion and Structural Response in
673 Alluvial Valleys. *Journal of Geotechnical and Geoenvironmental Engineering*, 125(5),
674 413–423.
- 675 Borcherdt, R. D., & Glassmoyer, G. (1992). On the characteristics of local geology and their
676 influence on ground motions generated by the Loma Prieta earthquake in the San Francisco
677 Bay region, California. *Bulletin of the Seismological Society of America*, 82(2), 603–641.
678 <https://doi.org/10.1785/BSSA0820020603>
- 679 Bradley, B. A. (2011). A framework for validation of seismic response analyses using
680 seismometer array recordings. *Soil Dynamics and Earthquake Engineering*, 31(3), 512–520.
681 <https://doi.org/10.1016/j.soildyn.2010.11.008>
- 682 Bradley, B. A. (2015). Systematic ground motion observations in the Canterbury earthquakes

- 683 and region-specific non-ergodic empirical ground motion modeling. *Earthquake Spectra*,
684 *31*(3), 1735–1761. [https://doi.org/https://doi.org/10.1193/053013EQS137M](https://doi.org/10.1193/053013EQS137M)
- 685 Bradley, B. A. (2019). On-going challenges in physics-based ground motion prediction and
686 insights from the 2010–2011 Canterbury and 2016 Kaikoura, New Zealand earthquakes.
687 *Soil Dynamics and Earthquake Engineering*, *124*, 354–364.
688 <https://doi.org/10.1016/j.soildyn.2018.04.042>
- 689 Brocher, T. M. (2005). Empirical Relations between Elastic Wavespeeds and Density in the
690 Earth’s Crust. *Bulletin of the Seismological Society of America*, *95*(6), 2081–2092.
691 <https://doi.org/10.1785/0120050077>
- 692 Brocher, T. M. (2008). Compressional and shear-wave velocity versus depth relations for
693 common rock types in northern California. *Bulletin of the Seismological Society of America*,
694 *98*(2), 950–968. <https://doi.org/10.1785/0120060403>
- 695 Cadet, H., Macau, A., Benjumea, B., Bellmunt, F., & Figueras, S. (2011). From ambient noise
696 recordings to site effect assessment: The case study of Barcelona microzonation. *Soil*
697 *Dynamics and Earthquake Engineering*, *31*(3), 271–281.
698 <https://doi.org/10.1016/J.SOILDYN.2010.07.005>
- 699 Campbell, K. W., & Bozorgnia, Y. (2014). NGA-West2 ground motion model for the average
700 horizontal components of PGA, PGV, and 5% damped linear acceleration response spectra.
701 *Earthquake Spectra*, *30*(3), 1087–1114. <https://doi.org/10.1193/062913EQS175M>
- 702 Castellaro, S., Mulargia, F., & Rossi, P. L. (2008). Vs30: Proxy for seismic amplification?
703 *Seismological Research Letters*, *79*(4), 540–543. <https://doi.org/10.1785/gssrl.79.4.540>
- 704 Chiou, B. S. J., & Youngs, R. R. (2014). Update of the Chiou and Youngs NGA model for the
705 average horizontal component of peak ground motion and response spectra. *Earthquake*
706 *Spectra*, *30*(3), 1117–1153. <https://doi.org/10.1193/072813EQS219M>
- 707 Cramer, C. H. (2003). Site-specific seismic-hazard analysis that is completely probabilistic.
708 *Bulletin of the Seismological Society of America*, *93*(4), 1841–1846.
709 <https://doi.org/10.1785/0120020206>

- 710 Cremen, G., Galasso, C., McCloskey, J., Barcena, A., Creed, M., Filippi, M. E., ... Trogrlić, R.
711 Š. (2023). A state-of-the-art decision-support environment for risk-sensitive and pro-poor
712 urban planning and design in Tomorrow's cities. *International Journal of Disaster Risk*
713 *Reduction*, 85, 103400. <https://doi.org/10.1016/j.ijdr.2022.103400>
- 714 Day, S. M., Graves, R., Bielak, J., Dreger, D., Larsen, S., Olsen, K. B., ... Ramirez-Guzman, L.
715 (2019). Model for Basin Effects on Long-Period Response Spectra in Southern California:
716 *Earthquake Spectra*, 24(1), 257–277. <https://doi.org/10.1193/1.2857545>
- 717 De Hoop, A. T. (1958). Representation theorems for the displacement in an elastic solid and their
718 application to elastodynamic diffraction theory . In *Technische Hogeschool, Delft,*
719 *Netherland*. Technische Hogeschoo.
- 720 Dolce, M., Masi, A., Marino, M., & Vona, M. (2003). Earthquake damage scenarios of the
721 building stock of Potenza (Southern Italy) including site effects. *Bulletin of Earthquake*
722 *Engineering*, 1(1), 115–140. <https://doi.org/10.1023/A:1024809511362>
- 723 Douglas, J. (2017). Ground motion prediction equations 1964-2019 (December 2019). *SED*
724 *Report SED/ENSI/R/01/20140911, October*, 1–651.
725 <http://www.gmpe.org.uk/gmpereport2014.pdf>
- 726 Douglas, J., & Aochi, H. (2008). A survey of techniques for predicting earthquake ground
727 motions for engineering purposes. *Surveys in Geophysics*, 29(3), 187–220.
728 <https://doi.org/10.1007/s10712-008-9046-y>
- 729 Douglas, J., & Edwards, B. (2016a). Recent and future developments in earthquake ground
730 motion estimation. *Earth-Science Reviews*, 160, 203–219.
731 <https://doi.org/10.1016/j.earscirev.2016.07.005>
- 732 Douglas, J., & Edwards, B. (2016b). Recent and future developments in earthquake ground
733 motion estimation. In *Earth-Science Reviews* (Vol. 160, pp. 203–219). Elsevier B.V.
734 <https://doi.org/10.1016/j.earscirev.2016.07.005>
- 735 Foti, S., Aimar, M., Ciancimino, A., & Passeri, F. (2019). Recent developments in seismic site
736 response evaluation and microzonation. *Proceedings of the 17th European Conference on*

- 737 *Soil Mechanics and Geotechnical Engineering, ECSMGE 2019.*
738 <https://doi.org/10.32075/17ECSMGE-2019-1117>
- 739 Frankel, A. (1993). Three-dimensional simulations of ground motions in the San Bernardino
740 Valley, California, for hypothetical earthquakes on the San Andreas Fault. *Bulletin of*
741 *Seismological Society of America*, 83(4), 1020–1041.
- 742 Freddi, F., Galasso, C., Cremen, G., Dall’Asta, A., Di Sarno, L., Giaralis, A., ... Woo, G. (2021).
743 Innovations in earthquake risk reduction for resilience: Recent advances and challenges.
744 *International Journal of Disaster Risk Reduction*, 60.
745 <https://doi.org/10.1016/j.ijdr.2021.102267>
- 746 García-Pérez, T., Ferreira, A. M. G., Yáñez, G., Iturrieta, P., & Cembrano, J. (2021). Effects of
747 topography and basins on seismic wave amplification: The Northern Chile coastal cliff and
748 intramountainous basins. *Geophysical Journal International*, 227(2), 1143–1167.
749 <https://doi.org/10.1093/gji/ggab259>
- 750 Geli, L., Bard, P. Y., & Jullien, B. (1988). The effect of topography on earthquake ground
751 motion: a review and new results. In *Bulletin - Seismological Society of America* (Vol. 78,
752 Issue 1, pp. 42–63). [https://doi.org/10.1016/0148-9062\(88\)90024-1](https://doi.org/10.1016/0148-9062(88)90024-1)
- 753 Gentile, R., Cremen, G., Galasso, C., Jenkins, L. T., Manandhar, V., Mentese, E. Y., ...
754 McCloskey, J. (2022). Scoring , selecting , and developing physical impact models for
755 multi- hazard risk assessment. *International Journal of Disaster Risk Reduction*, 82,
756 103365. <https://doi.org/https://doi.org/10.1016/j.ijdr.2022.103365>
- 757 Graves, R. W., & Pitarka, A. (2010). Broadband ground-motion simulation using a hybrid
758 approach. *Bulletin of the Seismological Society of America*, 100(5 A), 2095–2123.
759 <https://doi.org/10.1785/0120100057>
- 760 Graves, R. W., Pitarka, A., & Somerville, P. G. (1998). Ground-motion amplification in the
761 Santa Monica area: Effects of shallow basin-edge structure. *Bulletin of the Seismological*
762 *Society of America*, 88(5), 1224–1242. <https://doi.org/10.1785/bssa0880051224>
- 763 Hough, S. E., & Anderson, J. G. (1988). High-frequency Spectra Observed at Anza, California:

- 764 Implications for Q Structure. *Bulletin of the Seismological Society of America*, 78(2), 692–
765 707.
- 766 Hough, S. E., Martin, S. S., Gahalaut, V., Joshi, A., Landes, M., & Bossu, R. (2016). A
767 comparison of observed and predicted ground motions from the 2015 MW7.8 Gorkha,
768 Nepal, earthquake. *Natural Hazards*, 84(3), 1661–1684.
769 <https://doi.org/https://doi.org/10.1007/s11069-016-2505-8>
- 770 Jenkins, L. T., Creed, M. J., Tarbali, K., Muthusamy, M., Trogrlić, R. Š., Phillips, J. C., ...
771 McCloskey, J. (2023). Physics-based simulations of multiple natural hazards for risk-
772 sensitive planning and decision-making in expanding urban regions. *International Journal*
773 *of Disaster Risk Reduction*, 84, 103338.
774 <https://doi.org/https://doi.org/10.1016/j.ijdr.2022.103338>
- 775 Kaklamanos, J., Bradley, B. A., Thompson, E. M., & Baise, L. G. (2013). Critical parameters
776 affecting bias and variability in site-response analyses using KiK-net downhole array data.
777 *Bulletin of the Seismological Society of America*, 103(3), 1733–1749.
778 <https://doi.org/10.1785/0120120166>
- 779 Kamai, R., Abrahamson, N. A., & Silva, W. J. (2016). VS30 in the NGA GMPEs: Regional
780 differences and suggested practice. *Earthquake Spectra*, 32(4), 2083–2108.
781 <https://doi.org/10.1193/072615EQS121M>
- 782 Kiureghian, A. Der, & Ditlevsen, O. (2009). Aleatory or epistemic? Does it matter? *Structural*
783 *Safety*, 31(2), 105–112. <https://doi.org/10.1016/j.strusafe.2008.06.020>
- 784 Knopoff, L. (1956). Diffraction of Elastic Waves. *The Journal of the Acoustical Society of*
785 *America*, 28, 217. <https://doi.org/10.1121/1.1908247>
- 786 Kramer, S. L. (1996). *Geotechnical Earthquake Engineering*. Pearson Prentice-Hall, Upper
787 Saddle River, NJ, USA.
- 788 Kramer, S. L., & Mitchell, R. A. (2006). Ground Motion Intensity Measures for Liquefaction
789 Hazard Evaluation: *Earthquake Spectra*, 22(2), 413–438. <https://doi.org/10.1193/1.2194970>

- 790 Kuehn, N. M., Abrahamson, N. A., & Walling, M. A. (2019). Incorporating Nonergodic Path
791 Effects into the NGA-West2 Ground-Motion Prediction Equations. *Bulletin of the*
792 *Seismological Society of America* *Seismological Society of America*, 109(2), 575–585.
793 <https://doi.org/10.1785/0120180260>
- 794 Landwehr, N., Kuehn, N. M., Scheffer, T., & Abrahamson, N. (2016). A Nonergodic Ground-
795 Motion Model for California with Spatially Varying Coefficients. *Bulletin of the*
796 *Seismological Society of America*, 6, 2574–2583. <https://doi.org/10.1785/0120160118>
- 797 Lee, S. J., Komatitsch, D., Huang, B. S., & Tromp, J. (2009). Effects of topography on seismic-
798 wave propagation: An example from Northern Taiwan. *Bulletin of the Seismological Society*
799 *of America*, 99(1), 314–325. <https://doi.org/10.1785/0120080020>
- 800 Liu, P., Archuleta, R. J., & Hartzell, S. H. (2006). *Prediction of Broadband Ground-Motion Time*
801 *Histories : Hybrid Low / High- Frequency Method with Correlated Random Source*
802 *Parameters*. 96(6), 2118–2130. <https://doi.org/10.1785/0120060036>
- 803 Marafi, N. A., Eberhard, M. O., Berman, J. W., Wirth, E. A., & Frankel, A. D. (2017). Effects of
804 deep basins on structural collapse during large subduction earthquakes. *Earthquake Spectra*,
805 33(3), 963–997. <https://doi.org/10.1193/071916EQS114M>
- 806 Maufroy, E., Cruz-Atienza, V. M., & Gaffet, S. (2012). A robust method for assessing 3-D
807 topographic site effects: A case study at the LSBB underground laboratory, France.
808 *Earthquake Spectra*, 28(3), 1097–1115. <https://doi.org/10.1193/1.4000050>
- 809 Mazzieri, I., Stupazzini, M., Guidotti, R., & Smerzini, C. (2013). SPEED: SPectral Elements in
810 Elastodynamics with Discontinuous Galerkin: a non-conforming approach for 3D multi-
811 scale problems. *International Journal for Numerical Methods in Engineering*, 95(12), 991–
812 1010. <https://doi.org/10.1002/NME.4532>
- 813 Mazzieri, I., Stupazzini, M., Guidotti, R., Smerzini, C., Mazzieri, I., Stupazzini, M., ... Smerzini,
814 C. (2013). SPEED: SPectral Elements in Elastodynamics with Discontinuous Galerkin: a
815 non-conforming approach for 3D multi-scale problems. *IJNME*, 95(12), 991–1010.
816 <https://doi.org/10.1002/NME.4532>

- 817 Mcguire, R. K. (2008). Probabilistic seismic hazard analysis: Early history. *Earthquake*
818 *Engineering & Structural Dynamics*, 37, 329–338. <https://doi.org/10.1002/eqe.765>
- 819 Menteşe, E. Y., Cremen, G., Gentile, R., Galasso, C., Filippi, E. M., & McCloskey, J. (2023).
820 Future exposure modelling for risk-informed decision making in urban planning.
821 *International Journal of Disaster Risk Reduction*, 90, 103651.
822 <https://doi.org/10.1016/j.ijdr.2023.103651>
- 823 Mucciarelli, M., & Gallipoli, M. R. (2006). Comparison between Vs30 and other estimates of
824 site amplification in Italy. *First European Conference on Earthquake Engineering and*
825 *Seismology, September*, 270.
- 826 Nath, S. K., & Thingbaijam, K. K. S. (2011). Peak ground motion predictions in India: an
827 appraisal for rock sites. *Journal of Seismology*, 15(2), 295–315.
- 828 Ohsumi, T., Mukai, Y., & Fujitani, H. (2016). Investigation of Damage in and Around
829 Kathmandu Valley Related to the 2015 Gorkha, Nepal Earthquake and Beyond.
830 *Geotechnical and Geological Engineering*, 34(4), 1223–1245.
831 <https://doi.org/10.1007/s10706-016-0023-9>
- 832 Oral, E., Ayoubi, P., Ampuero, J. P., Asimaki, D., & Bonilla, L. F. (2022). Kathmandu Basin as
833 a local modulator of seismic waves: 2-D modelling of non-linear site response under
834 obliquely incident waves. *Geophysical Journal International*, 231(3), 1996–2008.
835 <https://doi.org/10.1093/gji/ggac302>
- 836 Paolucci, R., Mazzieri, I., Smerzini, C., & Stupazzini, M. (2014). Physics-Based Earthquake
837 Ground Shaking Scenarios in Large Urban Areas. *Geotechnical, Geological and*
838 *Earthquake Engineering*, 34, 331–359. https://doi.org/10.1007/978-3-319-07118-3_10
- 839 Pilz, M., Parolai, S., Stupazzini, M., Paolucci, R., & Zschau, J. (2011). Modelling basin effects
840 on earthquake ground motion in the Santiago de Chile basin by a spectral element code.
841 *Geophys. J. Int*, 187, 929–945. <https://doi.org/10.1111/j.1365-246X.2011.05183.x>
- 842 Pitilakis, K., Riga, E., Anastasiadis, A., Fotopoulou, S., & Karafagka, S. (2019). Towards the
843 revision of EC8: Proposal for an alternative site classification scheme and associated

- 844 intensity dependent spectral amplification factors. *Soil Dynamics and Earthquake*
845 *Engineering*, 126, 105137. [https://doi.org/https://doi.org/10.1016/j.soildyn.2018.03.030](https://doi.org/10.1016/j.soildyn.2018.03.030)
- 846 Poursartip, B., Fathi, A., & Tassoulas, J. L. (2020). Large-scale simulation of seismic wave
847 motion: A review. *Soil Dynamics and Earthquake Engineering*, 129, 105909.
848 <https://doi.org/10.1016/j.soildyn.2019.105909>
- 849 Rodriguez-Marek, A., Rathje, E. M., Bommer, J. J., Scherbaum, F., & Stafford, P. J. (2014).
850 Application of Single-Station Sigma and Site-Response Characterization in a Probabilistic
851 Seismic-Hazard Analysis for a New Nuclear Site. *Bulletin of Seismological Society of*
852 *America*, 104(4), 1601–1619. <https://doi.org/10.1785/0120130196>
- 853 Schmedes, J., Archuleta, R. J., & Lavalée, D. (2013). A kinematic rupture model generator
854 incorporating spatial interdependency of earthquake source parameters. *Geophysical*
855 *Journal International*, 192(3), 1116–1131. <https://doi.org/10.1093/gji/ggs021>
- 856 Sebastiano, D., Francesco, P., Salvatore, M., Roberto, I., Antonella, P., Giuseppe, L., ... Daniela,
857 F. (2019). Ambient noise techniques to study near-surface in particular geological
858 conditions: A brief review. In *Innovation in Near-Surface Geophysics: Instrumentation,*
859 *Application, and Data Processing Methods* (pp. 419–460). Elsevier Inc.
860 <https://doi.org/10.1016/B978-0-12-812429-1.00012-X>
- 861 Semblat, J. F., Kham, M., Parara, E., Bard, P. Y., Pitilakis, K., Makra, K., & Raptakis, D. (2005).
862 Seismic wave amplification: Basin geometry vs soil layering. *Soil Dynamics and*
863 *Earthquake Engineering*, 25(7–10), 529–538. <https://doi.org/10.1016/j.soildyn.2004.11.003>
- 864 Sextos, A., De Risi, R., Pagliaroli, A., Foti, S., Passeri, F., Ausilio, E., ... Zimmaro, P. (2018).
865 Local site effects and incremental damage of buildings during the 2016 Central Italy
866 Earthquake sequence. *Earthquake Spectra*, 34(4), 1639–1669.
867 <https://doi.org/10.1193/100317EQS194M>
- 868 Shi, J., & Asimaki, D. (2017). From Stiffness to Strength: Formulation and Validation of a
869 Hybrid Hyperbolic Nonlinear Soil Model for Site-Response Analyses. *Bulletin of the*
870 *Seismological Society of America*, 107(3), 1336–1355. <https://doi.org/10.1785/0120150287>

- 871 Smerzini, C., Paolucci, R., & Stupazzini, M. (2011). Comparison of 3D, 2D and 1D numerical
872 approaches to predict long period earthquake ground motion in the Gubbio plain, Central
873 Italy. *Bulletin of Earthquake Engineering*, 9(6), 2007–2029. [https://doi.org/10.1007/s10518-](https://doi.org/10.1007/s10518-011-9289-8)
874 011-9289-8
- 875 Smerzini, C., & Villani, M. (2012). Broadband numerical simulations in complex near-field
876 geological configurations: The case of the 2009 Mw 6.3 L'Aquila earthquake. *Bulletin of*
877 *the Seismological Society of America*, 102(6), 2436–2451.
878 <https://doi.org/10.1785/0120120002>
- 879 Spudich, P., Bayless, J. R., Baker, J., Chiou, B. S. J., Rowshandel, B., Shahi, S., & Somerville,
880 P. (2013). Final Report of the NGA-West2 Directivity Working Group. In *Pacific*
881 *Engineering Research Center Report* (Issue 09).
- 882 Stewart, J. P., Afshari, K., & Goulet, C. A. (2017). Non-ergodic site response in seismic hazard
883 analysis. *Earthquake Spectra*, 33(4), 1385–1414. <https://doi.org/10.1193/081716EQS135M>
- 884 Stirling, M. W. (2014). The Continued Utility of Probabilistic Seismic-Hazard Assessment. In
885 *Earthquake Hazard, Risk and Disasters* (pp. 359–376). Elsevier Inc.
886 <https://doi.org/10.1016/B978-0-12-394848-9.00013-4>
- 887 Stirling, M. W., McVerry, G., Gerstenberger, M., Litchfield, N., Van Dissen, R., Berryman, K.,
888 ... Jacobs, K. (2012). National seismic hazard model for New Zealand: 2010 update.
889 *Bulletin of the Seismological Society of America*, 102(4), 1514–1542.
890 <https://doi.org/10.1785/0120110170>
- 891 Tabora, R., Bielak, J., & Restrepo, D. (2012). Earthquake Ground-Motion Simulation including
892 Nonlinear Soil Effects under Idealized Conditions with Application to Two Case Studies.
893 *Seismological Research Letters*, 83(6), 1047–1060. <https://doi.org/10.1785/0220120079>
- 894 Tabora, R., Roten, D., & Diego, S. (2014). Physics-Based Ground-Motion Simulation. In
895 *Encyclopedia of Earthquake Engineering* (Issue January, pp. 1–33).
896 <https://doi.org/10.1007/978-3-642-36197-5>
- 897 Torre, C. A. de la, Bradley, B. A., & Lee, R. L. (2020). Modeling nonlinear site effects in

- 898 physics-based ground motion simulations of the 2010–2011 Canterbury earthquake
899 sequence: *Earthquake Spectra*, 36(2), 856–879. <https://doi.org/10.1177/8755293019891729>
- 900 Tsai, C. C., Kishida, T., & Lin, W. C. (2021). Adjustment of site factors for basin effects from
901 site response analysis and deep downhole array measurements in Taipei. *Engineering*
902 *Geology*, 285(June 2020), 106071. <https://doi.org/10.1016/j.enggeo.2021.106071>
- 903 UN-Habitat. (2022). World Cities Report 2020: Envisaging the Future of Cities. In *World Cities*
904 *Report 2020: Envisaging the Future of Cities*. UN.
- 905 UNISDR, U. (2015). Sendai framework for disaster risk reduction 2015-2030. *Proceedings of*
906 *the 3rd United Nations World Conference on DRR*.
- 907 Wang, C., Cremen, G., Gentile, R., & Galasso, C. (2023). Design and assessment of pro-poor
908 financial soft policies for expanding cities. *International Journal of Disaster Risk*
909 *Reduction*, 85(December 2022), 103500. <https://doi.org/10.1016/j.ijdrr.2022.103500>
- 910 Wang, G., Du, C., Huang, D., Jin, F., Koo, R. C. H., & Kwan, J. S. H. (2018). Parametric models
911 for 3D topographic amplification of ground motions considering subsurface soils. *Soil*
912 *Dynamics and Earthquake Engineering*, 115(September 2017), 41–54.
913 <https://doi.org/10.1016/j.soildyn.2018.07.018>
- 914 Yomogida, K., & Etgen, J. T. (1993). 3-D wave propagation in the Los Angeles Basin for the
915 Whittier-Narrows earthquake. *Bulletin of the Seismological Society of America*, 83(5),
916 1325–1344. <https://doi.org/10.1086/622062>
- 917 Zhu, C., Thambiratnam, D., & Gallage, C. (2018). Statistical analysis of the additional
918 amplification in deep basins relative to the 1D approach. *Soil Dynamics and Earthquake*
919 *Engineering*, 104, 296–306. <https://doi.org/10.1016/j.soildyn.2017.09.003>